Progress In Electromagnetics Research C, Vol. 136, 175–187, 2023

Comparative Analysis of Auxiliary Teeth Flux Reversal PM Machines with Different Magnetization Modes

Kun Yang, Libing Jing*, Zhangtao Kui, and Zeyu Min

Abstract—Flux reversal permanent magnet machine (FRPMM) has been widely used because of its high efficiency, simple structure and high fault tolerance. However, the torque of the FRPMM is restricted by its longer equivalent length of air gap. To further improve its torque density, this paper presents two novel FRPMMs with auxiliary teeth and different magnetization modes. Both machines use auxiliary teeth without permanent magnet (PM), and both machines have three PM blocks on each main tooth. The difference between the two machines is that they have different orders of arrangement of PM. The design parameters of the two machines are optimized based on genetic algorithm (GA). Finally, the back EMF and torque of the two machines are compared with the conventional FRPMM to show the superiority of the two machines. At the same time, the other important performances of the two machines are compared and analyzed, and their respective advantages and disadvantages are obtained as a reference for selecting the respective appropriate application scenarios.

1. INTRODUCTION

The permanent magnet (PM) of the conventional rotor PM machine is located on a high-speed rotating rotor, which makes it difficult to cool and thus faces the risk of demagnetization under high temperatures. At the same time, the weak mechanical strength of the rotor leads to poor reliability of the machine. Because of overcoming some inherent shortcomings of the conventional rotor PM machine, the novel stator PM machine has received more and more attention [1]. The winding and PM of the stator PM machine are on the stator and no longer rotate with the rotor, which gives them the advantage of convenient direct heat dissipation.

As a stator PM machine, the rotor of a flux reversal permanent magnet machine (FRPMM) is a simple salient pole structure like the rotor of other stator PM machines, which leads to its strong robustness, high reliability, and suitability for high-speed operation. The installation of the PM of an FRPMM is like a surface-mounted rotor PM machine, but the difference is that the PM of an FRPMM is on the surface of the stator teeth, which can be installed more conveniently. Due to these significant advantages, FRPMMs have been successfully applied in many fields such as electric vehicles and new energy power generation [2]. Many researchers have done a lot of excellent work on FRPMMs.

In [3], an analytical design method of FRPMM was established, and the effect of the key parameters in the size equation on torque density was studied simultaneously. In [4], the back electromagnetic field (EMF) of an FRPMM was researched by the magnetic field modulation theory. In [5], the principle of pole-slot combination considering both magnetic flux leakage effect and magnetization mode was proposed, and the impact of pole-slot combination on key performances was studied. In [6], the back EMF of FRPMMs with different coil pitches and magnetization modes was studied. In [7], the FRPMMs with ring windings and concentrated windings were compared and analyzed, and the FRPMM with ring

Received 26 June 2023, Accepted 9 August 2023, Scheduled 19 August 2023

* Corresponding author: Libing Jing (jinglibing163@163.com).

The authors are with the College of Electrical Engineering and New Energy, Hubei Provincial Engineering Technology Research Center for Microgrid, China Three Gorges University, Yichang 443002, China.

windings showed better electromagnetic performances. In [8], an FRPMM with asymmetric stator teeth was proposed, which effectively improved torque quality and power factor. In further research, a hybrid analytical model of the FRPMM with asymmetric stator teeth is established [9]. In [10], a doubly fed FRPMM with higher torque density and better fault tolerance was proposed. In [11, 12], the optimal quantities of PM blocks and the optimal magnetization sequence were studied. In [13], an FRPMM with evenly distributed PM was proposed, which has an obvious improvement in the torque density, cogging torque, and torque ripple. In [14], an FRPMM with a Halbach array PM in stator slots was proposed, which effectively improved the average torque while reducing the torque ripple. In [15], a spoke array FRPMM was proposed, which had advantages in average torque, power factor, efficiency, and torque ripple. In a further study, the effect of the quantities and form of PM blocks on the performances of the spoke array FRPMM was analyzed [16].

Consequent pole topology was used in FRPMMs to increase torque density and reduce PM consumption, but it usually also makes the machine have greater torque ripple than conventional FRPMM [17, 18]. To increase torque and reduce the PM consumption while reducing torque ripple, this paper presents and compares two novel FRPMMs with auxiliary teeth.

In Section 2, the topology and working principle are introduced. In Section 3, the design parameters of the two machines are optimized based on the genetic algorithm (GA). In Section 4, the electromagnetic performances of the two machines are compared and analyzed, and the key electromagnetic performances of the two machines are compared with the conventional FRPMM. In Section 5, the conclusion is given.

2. TOPOLOGY AND WORKING PRINCIPLE

2.1. Topology

The topologies of the machines are shown in Figure 1. Their rotors are simple salient pole structures like the conventional FRPMM. The stators of both machines change half of the teeth into auxiliary teeth without PM. At the same time, there are three PM blocks with alternating polarity on each main tooth of the two novel machines, which is different from the conventional FRPMM with two opposite polarity PM blocks on each stator tooth. The difference between the two machines is that the PM of machine A shown in Figure 1(a) is arranged in order of 'NSN-SNS', while the PM of machine B shown in Figure 1(b) is arranged in order of 'NSN-NSN'. The different PM arrangements make them have different winding connection modes. The star of the slots of the two machines is shown in Figure 2.

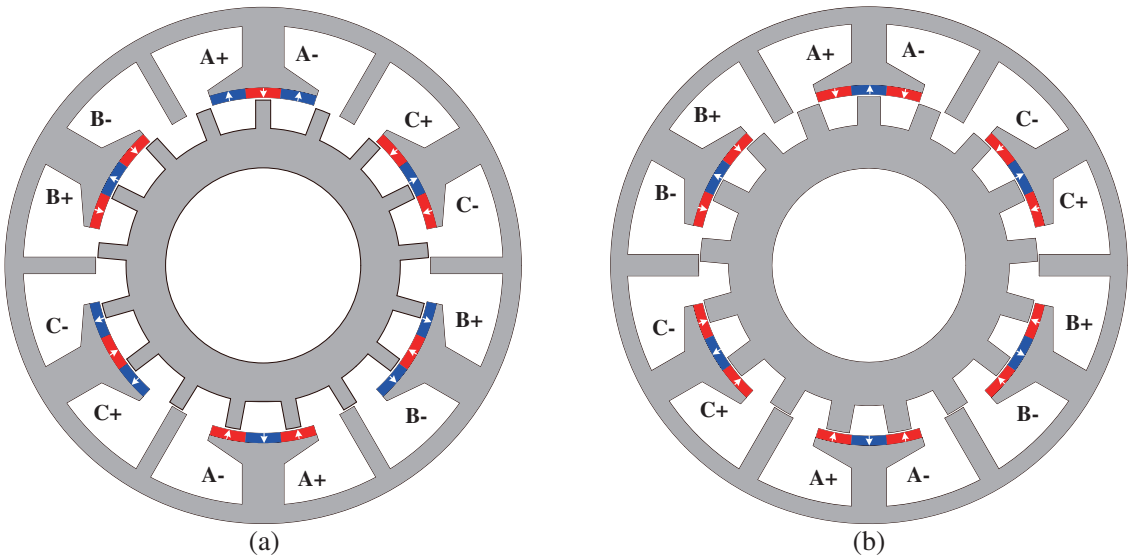

Figure 1. The topologies of machines. (a) Machine A; (b) Machine B.

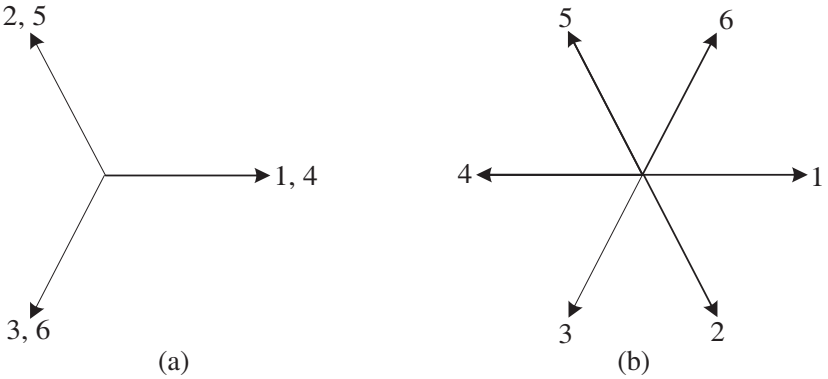

Figure 2. The star of slots. (a) Machine A; (b) Machine B.

2.2. Working Principle

FRPMMs are typical magnetic field modulation machines. The static magnetomotive force produced by the static PM is modulated by the rotating rotor teeth to generate a rotating air gap flux density. Hence, a miniature change of the rotor position will bring about a significant change in the magnetic circuit, resulting in a rapid change in the size and direction of the flux linkage, and then induced back EMF. Inputting the corresponding frequency current in the stator winding will produce stable electromagnetic

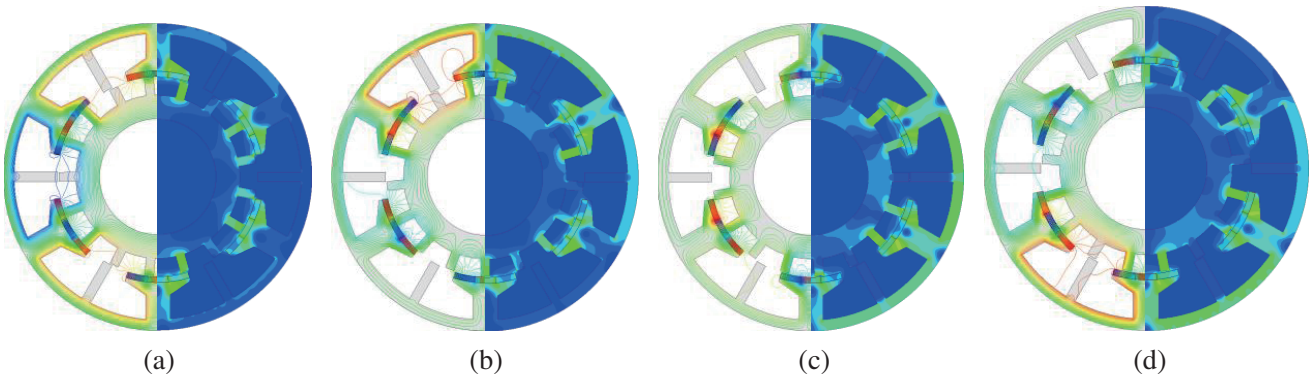

Figure 3. Field distributions of machine A at different rotor positions. (a) Electrical angle 0°. (b) Electrical angle 90°. (c) Electrical angle 180°. (d) Electrical angle 270°.

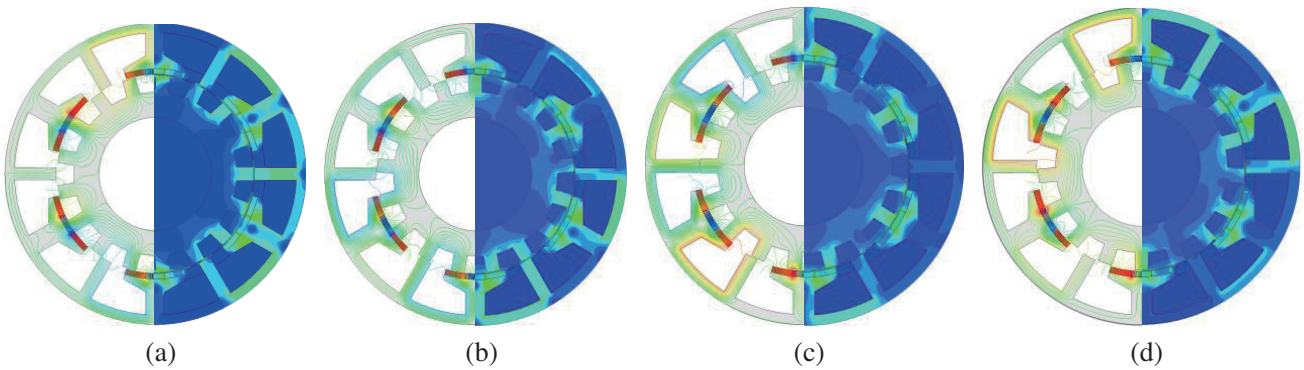

Figure 4. Field distributions of machine B at different rotor positions. (a) Electrical angle 0°. (b) Electrical angle 90°. (c) Electrical angle 180°. (d) Electrical angle 270°.

torque. In an electrical cycle, the open circuit magnetic fields of two machines at different electrical angles are shown in Figure 3 and Figure 4, respectively. The phase flux linkages of the two machines in one electrical cycle are reversed.

According to magnetic field modulation theory [19], the winding pole-pairs P, stator slot number N_s, and rotor tooth number N_r of the FRPMM should satisfy:

$$P = \min\left\{ |nNs \pm mN_r| \,; \frac{Ns}{GCD(Ns, P)} = 3j \right\} \tag{1}$$

where $n = 1, 2, 4, 5 \ldots k$, $k \neq 3i$ $(i = 1, 2, 3 \ldots)$, $m = 1, 2, 3 \ldots$, $j = 1, 2, 3 \ldots$, GCD denotes the greatest common divisor.

3. PARAMETRIC OPTIMIZATION

To comprehensively consider the interaction between parameters and meet the optimization requirements of objectives, multi-objective global optimization based on GA is adopted [20]. The selected optimization objectives are maximum average torque and minimum torque ripple. The performances of the two machines, the axial length, outer diameter, current excitation, material, and speed of the two machines are determined and maintained the same before optimization, as listed in Table 1. The parameterized model is shown in Figure 5.

Table 1. Design parameters of the machines.

Parameter	Value
axial length	60 mm
outer diameter	60 mm
current	7 A
speed	1000 rpm
PM material	NdFeB
steel material	DW315-50

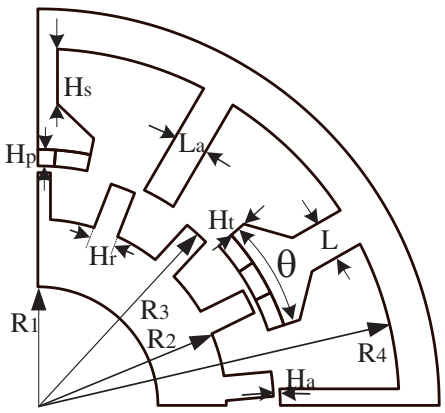

Figure 5. Parameterized model.

After determining the optimization objectives and establishing the parametric model, a reasonable range of design parameters is selected. Then the experimental matrix is established based on the central composite design (CCD) method, and the response value is obtained by finite element analysis. The response values of the experimental results are fitted, and the response surface of each optimization

target is achieved. Then, the design parameters are optimized based on GA. Finally, the optimal value of the design parameters is determined according to the optimization results. The flowchart for optimization is shown in Figure 6. The optimization results are shown in Figure 7. The scope and ultimate values of design parameters based on the optimization results are listed in Table 2.

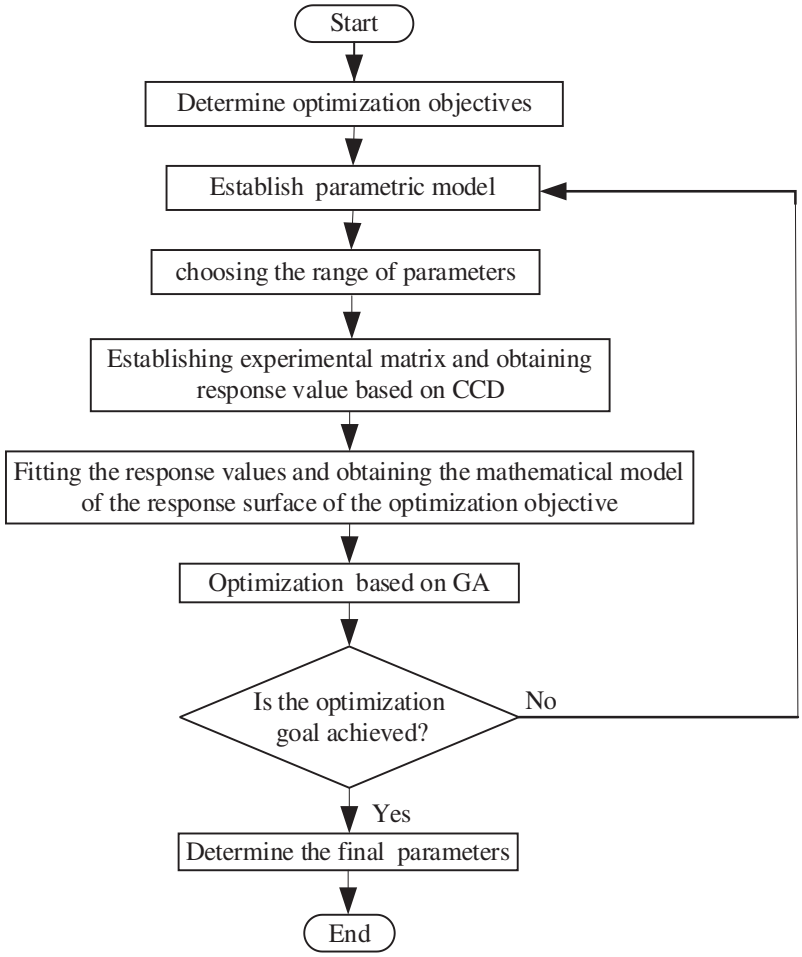

Figure 6. Flow chart of optimization.

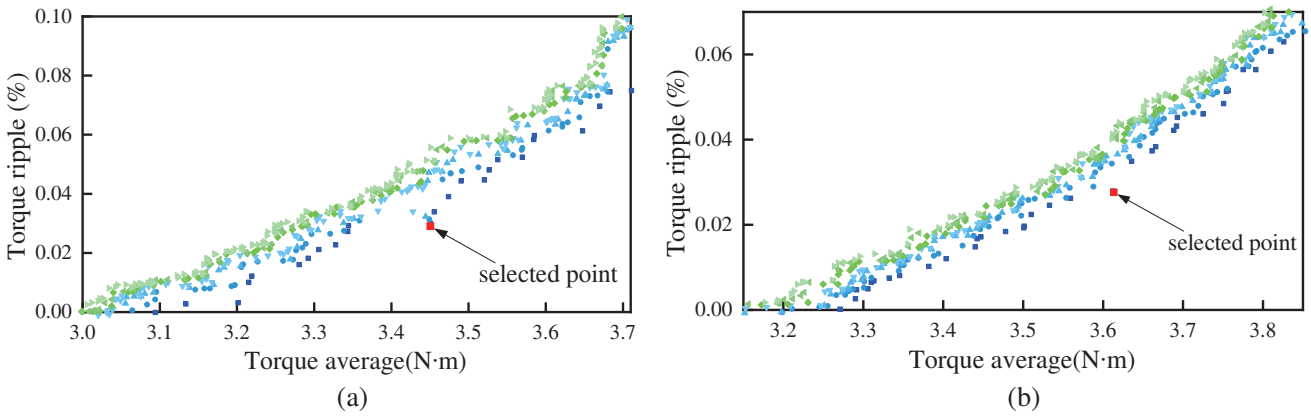

Figure 7. Optimization results. (a) Machine A; (b) Machine B.

Table 2. Scope and ultimate value of parameters.

Parameter	Range	Machine A	Machine B
The inner radius of rotor R_1/mm	20–25	22.69	22.57
The outer radius of rotor yoke R_2/mm	30–35	31.88	32.58
The outer radius of rotor R_3/mm	37–42	38.48	39.16
width of rotor teeth H_r/mm	3–6	3.49	5.29
air gap length H_a/mm	0.4–0.6	0.54	0.51
The thickness of PM H_p/mm	2–3	2.3	2.21
the radian of stator teeth θ/deg.	30–40	35.02	34.39
The thickness of stator yoke H_t/mm	1–3	1.3	1.98
length of main stator teeth H_s/mm	7–10	9.47	8.98
width of main stator teeth L/mm	7–10	9.65	8.04
width of auxiliary teeth L_a/mm	3–7	3.78	4.9
The inner radius of stator yoke R_4/mm	55–57	55.81	56.17

4. COMPARISON OF ELECTROMAGNETIC PERFORMANCE

4.1. Flux Density

The air gap flux density is shown in Figure 8. The two machines have different pole pairs of air gap magnetic fields. Machine A is 9, and machine B is 12. The reason is that although machine B also uses 18 PM blocks, its auxiliary teeth automatically play the role of a polar PM, which is corresponding to half of the PM using the consequent pole topology. The amplitude of the flux density of machine A is 1.168 T, and machine B is 1.011 T. The magnitude of the flux density of machine A is larger than that of machine B. However, since machine B has a smaller magnetic flux leakage, machine B has a larger amplitude of flux linkage, as shown in Figure 9. The amplitude of flux linkage of machine A is 0.0136 Wb, and that of machine B is 0.0148 Wb, with machine A 8.8% lower than machine B. The harmonic spectrum of the air gap flux density is shown in Figure 8(b). The main harmonics of machine A are the 5th, 12th, 18th, 29th, and 48th, while the main harmonics of machine B are the 3rd, 9th, 15th, 21st, and 45th.

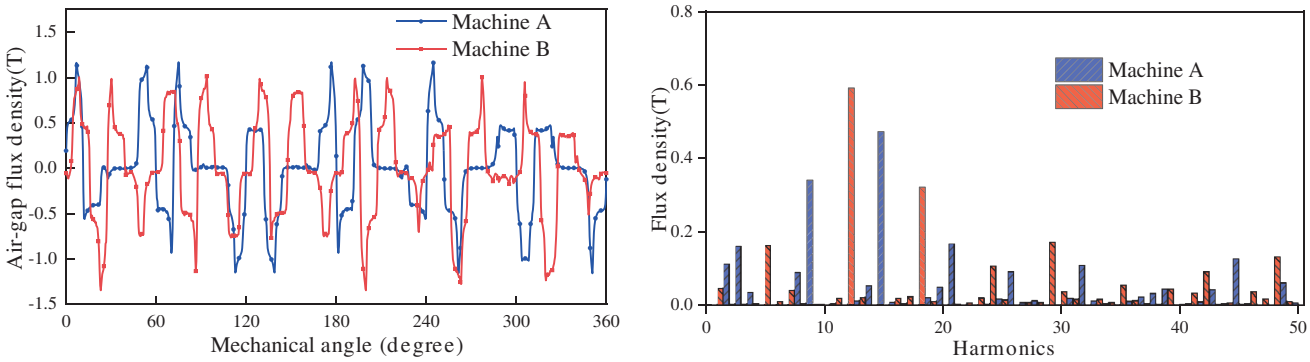

Figure 8. Air gap flux density. (a) Flux density distribution; (b) Harmonic spectra.

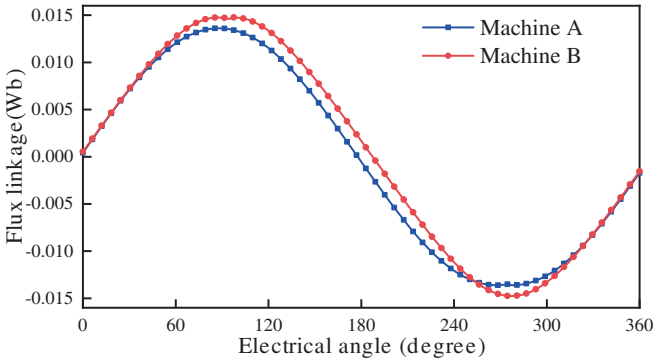

Figure 9. Flux linkage.

4.2. Back EMF

To demonstrate the advantages of the two presented machines, the back EMF and torque of them are compared with conventional FRPMM. The classical 12-slot and 17-pole FRPMM is selected as the comparison object, and its topology is shown in Figure 10.

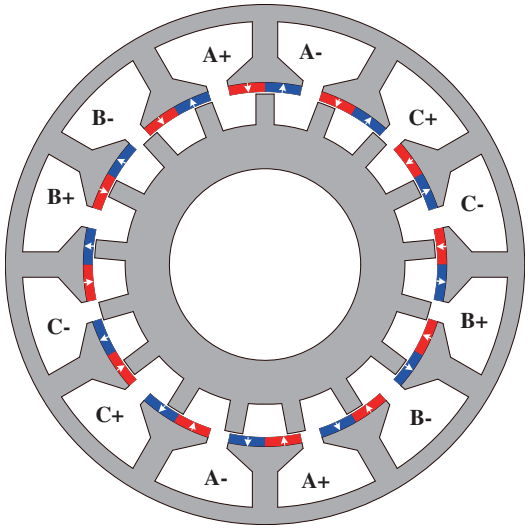

Figure 10. Topology of the conventional FRPMM.

For equitable comparison, the conventional FRPMM is also globally optimized under the parameters in Table 1. The back EMF of the two machines and the conventional FRPMM is shown in Figure 11. The amplitude of the back EMF of machine A is 23.6 V; that of machine B is 23.2 V, and that of the conventional FRPMM is 18.8 V. Compared with the conventional FRPMM, machine A and machine B are increased by 25.5% and 23.4%, respectively. Meanwhile, the total harmonic distortion (THD) rate is used to measure the sinusoidal degree of the back EMF waveform. The higher the sinusoidal degree is, the smaller the THD is, expressed as:

$$\mathrm{THD} = \frac{\sqrt{\sum_{i=2}^{n} B_{\delta i}^2}}{B_{\delta 1}} \times 100\% \tag{2}$$

where i is the harmonic order, and B_δ is the amplitude of each harmonic.

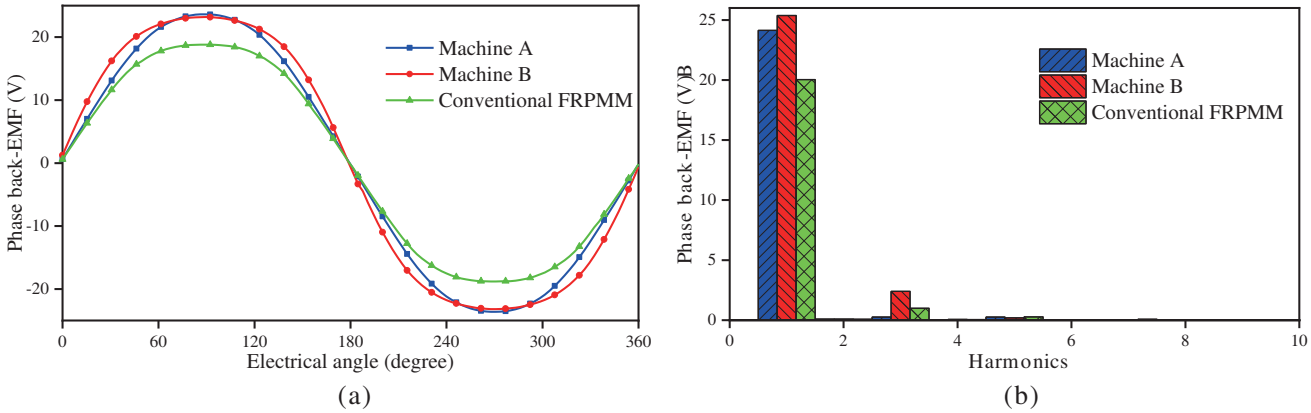

Figure 11. Back EMF. (a) Waveform; (b) Harmonic spectra.

The THD of machine A is 1.61%; the THD of machine B is 9.78%; and the THD of conventional FRPMM is 5.38%. The back EMF waveform of machine A is the most sinusoidal, followed by conventional FRPMM and machine B again.

4.3. Torque

According to Maxwell stress tensor method [21], the torque is expressed as:

$$T_{\text{em}} = \frac{R_{\text{e}}^2 L_{ef}}{\mu_0} \int_0^{2\pi} B_r B_t d\theta \tag{3}$$

where R_e is the radius of the air gap; L_{ef} is the effective axial length; μ is the permeability of the vacuum; B_r and B_t are the radial and tangential flux densities.

The torque ripple T_{pkavg} is defined as:

$$T_{pkavg} = \frac{T_{\max} - T_{\min}}{T_{avg}} \tag{4}$$

where $T_{\max}$ is the maximum of electromagnetic torque, $T_{\min}$ the minimum of electromagnetic torque, and T_{avg} the average value of electromagnetic torque.

The electromagnetic torques of the two machines and the conventional FRPMM are shown in Figure 12. T_{em} of machine A is 3.43 Nm; that of machine B is 3.59 Nm; and that of conventional FRPMM is 2.87 Nm. The average torques of machine A and machine B are increased by 19.5%

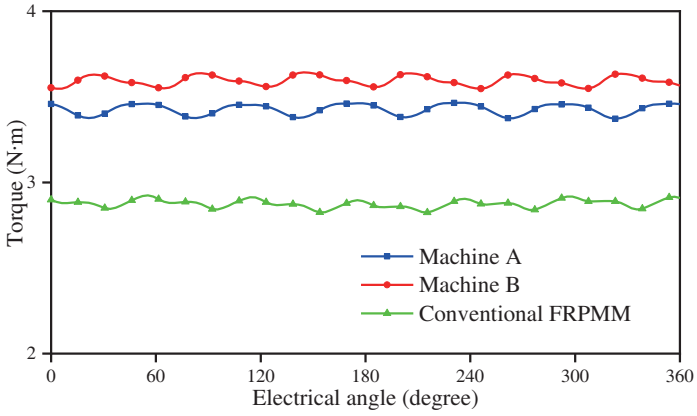

Figure 12. Torque.

and 25.1%, respectively, compared with the conventional FRPMM. Both machines have higher torque density. T_{pkavg} of machine A is 2.70%; that of machine B is 2.65%; and that of conventional FRPMM is 3.49%. The torque ripples of machine A and machine B are reduced by 22.6% and 24.1%, respectively, compared to conventional FRPMM. At the same time, PM consumptions of machines A and machines B are reduced by 20.5% and 24.1%, respectively, compared to conventional FRPMM. This shows that the two machines can have greater output torque per unit volume of PM and that both machines have higher average torque, lower torque ripple, and lower PM consumption than conventional FRPMM.

4.4. Overload Capability

To analyze the overload capacity of two machines, the torque and current curves are shown in Figure 13. Machine B is easier to reach saturation than machine A, and machine A has stronger overload capacity. Machine B has a stronger armature reaction leading to this result. However, in a wide load range, machine B can still provide higher or similar torque than machine A.

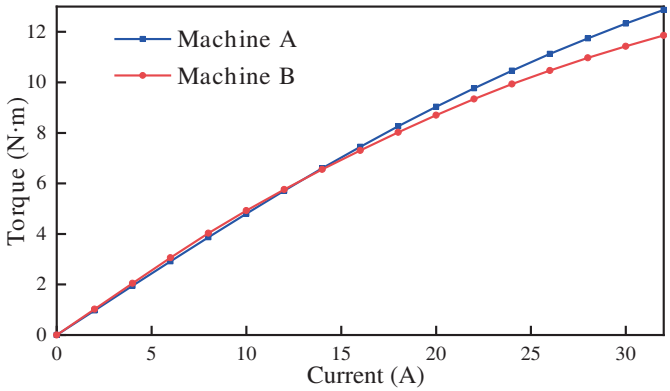

Figure 13. Torque versus current curves.

4.5. Fault Tolerant Capability

The self-inductance and mutual inductance are shown in Figure 14. To analyze the fault tolerance, the coupling coefficient K is defined as follows:

$$K = \frac{L_m}{L_a} \tag{5}$$

where L_m is the mutual inductance, and L_a is the self-inductance.

L_a of machine A is 993 μH; that of L_m of machine A is −184.3 μH; that of of machine B is 1332.8 μH; and L_m of machine B is 6 μH. The coupling coefficient K of machine A (0.1856) is much larger than that of machine B (0.0045). This indicates that the phase of machine A is tightly coupled, while the phase of machine B is basically decoupled, which is very conducive to fault tolerance. The main reason is that the coil of machine B is reversely connected, and it is easy which makes it have much better fault tolerance than machine A.

4.6. Power Factor

The power factor (PF) can be obtained according to the phasor diagram under $I_d = 0$ control in Figure 15 [13]:

$$PF = \frac{1}{\sqrt{1 + (\omega_e I_s L_s / E0)^2}} = \frac{1}{\sqrt{1 + (I_s L_s / \psi_m)^2}} \tag{6}$$

where I_s is the stator current, ω_e the electrical angular speed, L_s the synchronous inductance, E_0 the back EMF, and ψ_m the no load phase flux linkage.

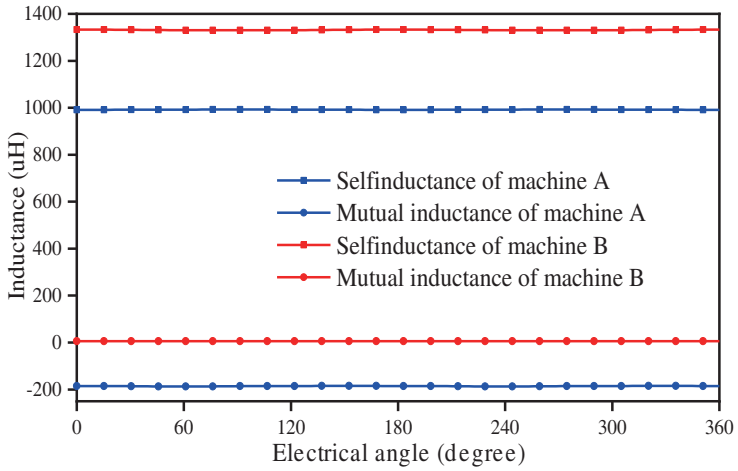

Figure 14. Inductance.

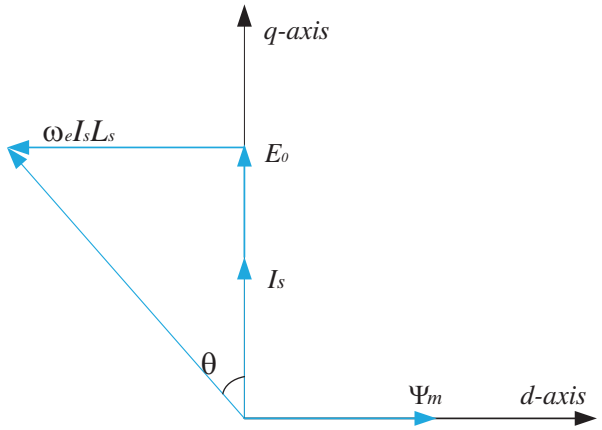

Figure 15. Phasor diagram under $Id = 0$.

The values of synchronous inductance, phase linkage, and PF are list in Table 3. The PF of machine A is 0.7563, which is 1.7% higher than the PF of machine B 0.7439. Although the flux linkage of machine A is small, it also has a small synchronous inductance, which makes the difference of the PF of the machine A and machine B very small.

Table 3. The synchronous inductance, phase linkage, and PF.

	Unit	Machine A	Machine B
synchronous inductance	mH	1.1764	1.3256
phase linkage	Wb	0.0136	0.0148
PF		0.7563	0.7439

4.7. Loss and Efficiency

The core loss, eddy current loss, and copper loss of machine A and machine B are shown in Figure 16, Figure 17, and Figure 18.

The core loss of machine A is 10.383 W, and that of machine B is 18.105 W. Machine B has a larger core loss. The eddy current loss of machine A is 5.966 W, and that of machine B is 6.035 W. And the copper losses of machine A and machine B are 2.36 W and 2.443 W, respectively.

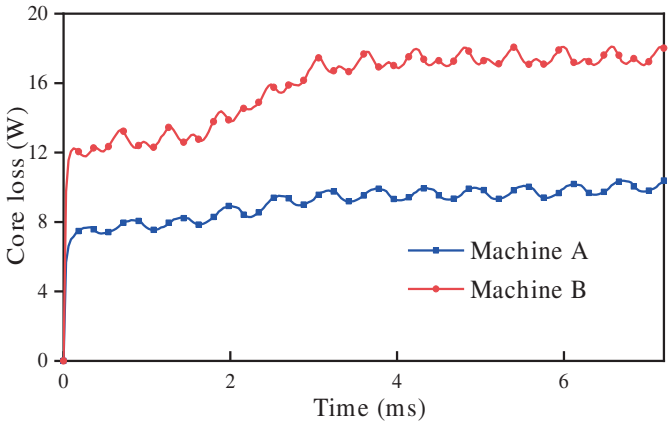

Figure 16. Core loss.

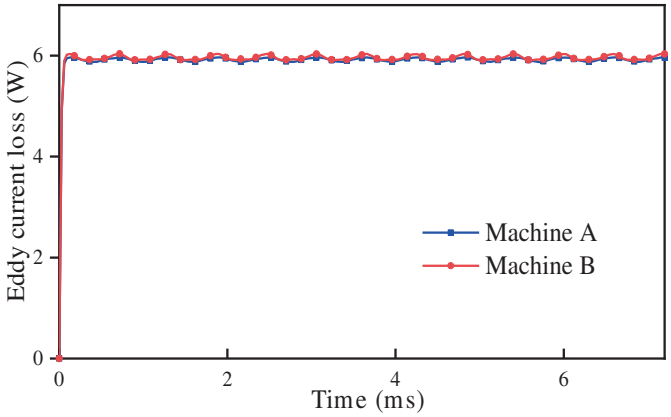

Figure 17. Eddy current loss.

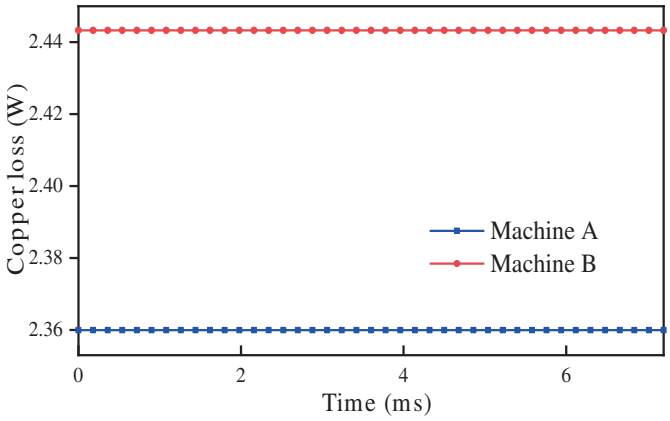

Figure 18. Copper loss.

The efficiency η of the two machines can be obtained:

$$\eta = \frac{P}{P + P_{core} + P_{eddy} + P_{copper}} \tag{7}$$

where P is the output power, P_{core} the core loss, P_{eddy} the eddy current loss, and P_{copper} the copper loss.

Output power, various losses, and efficiency of two machines are listed in Table 4. The total loss of machine A is 18.71 W, and that of machine B is 26.58 W, with machine B about a third higher than machine A. The efficiency of machine A is 94.95%; the efficiency of machine B is 93.38%; machine A has higher efficiency.

Table 4. Output power, various losses, and efficiency.

	Unit	Machine A	Machine B
core loss	W	10.383	18.105
eddy current loss	W	5.966	6.035
copper loss	W	2.36	2.443
total loss	W	18.71	26.58
output power	W	359.19	376
efficiency		94.95%	93.38%

5. CONCLUSION

Two novel auxiliary teeth FRPMMs with different PM arrangements are presented in this paper, and the design parameters of the two machines are globally optimized based on GA. The key performances of the two machines are compared with the conventional FRPMM. At the same time, more performances of the two machines are compared and analyzed. The contributions of this study are summarized as follows.

(1) Machine A and machine B respectively have 25.5% and 23.4% higher back EMF, 20.5% and 24.1% higher average torque, 22.6% and 24.1% lower torque ripple, 19.5% and 24.1% less PM consumption than the conventional FRPMM, which proves the advantages of the two machines.

(2) The results demonstrate that machine A has a more sinusoidal back EMF waveform closer to the sine wave, better overload capacity, higher power factor, higher efficiency; machine B has higher average torque, better fault tolerance; and the two machines have similar amplitude of back EMF and similar torque ripple. This provides a reference for the two machines to choose their respective suitable application scenarios.

REFERENCES

1. Cheng, M., W. Hua, J. Zhang, and W. Zhao, "Overview of stator-permanent magnet brushless machines," *IEEE Trans. Ind. Electron.*, Vol. 58, No. 11, 5087–5101, Nov. 2011.
2. Gao, Y., D. Li, R. Qu, X. Fan, J. Li, and H. Ding, "A novel hybrid excitation flux reversal machine for electric vehicle propulsion," *IEEE Trans. Veh. Technol.*, Vol. 67, No. 1, 171–182, Jan. 2018.
3. Gao, Y., D. Li, R. Qu, and J. Li, "Design procedure of flux reversal permanent magnet machines," *IEEE Trans. Ind. Appl.*, Vol. 53, No. 5, 4232–4241, Sep.–Oct. 2017.
4. Zhu, X., W. Hua, W. Wang, and W. Huang, "Analysis of back-EMF in flux-reversal permanent magnet machines by air gap field modulation theory," *IEEE Trans. Ind. Electron.*, Vol. 66, No. 5, 3344–3355, 2019.
5. Zhu, X. and W. Hua, "Stator-slot/rotor-pole pair combinations of flux-reversal permanent magnet machine," *IEEE Trans. Ind. Electron.*, Vol. 66, No. 9, 6799–6810, Sep. 2019.
6. Hua, W., X. Zhu, and Z. Wu, "Influence of coil pitch and stator-slot/rotor-pole combination on back EMF harmonics in flux-reversal permanent magnet machines" *IEEE Trans. Energy Conversion.*, Vol. 33, No. 3, 1330–1341, 2018.
7. Li, H., Z. Zhu, and H. Hua, "Comparative analysis of flux reversal permanent magnet machines with toroidal and concentrated windings," *IEEE Trans. Ind. Electron.*, Vol. 67, No. 7, 5278–5290, 2020.

8. Yang, H., H. Lin, Z. Zhu, S. Lyu, and Y. Liu, "Design and analysis of novel asymmetric-stator-pole flux reversal pm machine," *IEEE Trans. Ind. Electron.*, Vol. 67, No. 1, 101–114, 2020.
9. Liu, W., H. Yang, H. Lin, and L. Qin, "Hybrid analytical modeling of air-gap magnetic field in asymmetric-stator-pole flux reversal permanent magnet machine considering slotting effect," *IEEE Trans. Ind. Electron.*, Vol. 69, No. 2, 1739–1749, Feb. 2022.
10. Wu, L., Y. Zheng, Y. Fang, and X. Huang, "Novel fault-tolerant doubly fed flux reversal machine with armature windings wound on both stator and rotor teeth," *IEEE Trans. Ind. Electron.*, Vol. 68, No. 6, 4780–4789, 2021.
11. Li, H. and Z. Zhu, "Optimal number of magnet pieces of flux reversal permanent magnet machines," *IEEE Trans. Energy Convers.*, Vol. 34, No. 2, 889–898, 2019.
12. Li, H. and Z. Zhu, "Influence of adjacent teeth magnet polarities on the performance of flux reversal permanent magnet machine," *IEEE Trans. Ind. Appl.*, Vol. 55, No. 1, 354–365, Jan.–Feb. 2019.
13. Li, D., Y. Gao, R. Qu, J. Li, Y. Huo, and H. Ding, "Design and analysis of a flux reversal machine with evenly distributed permanent magnets," *IEEE Trans. Ind. Appl.*, Vol. 54, No. 1, 172–183, 2018.
14. Xie, K., D. Li, R. Qu, Z. Yu, Y. Gao, and Y. Pan, "Analysis of a flux reversal machine with quasi-halbach magnets in stator slot opening," *IEEE Trans. Ind. Appl.*, Vol. 55, No. 2, 1250–1260, 2019.
15. Qu, H. and Z. Zhu, "Analysis of spoke array permanent magnet flux reversal machines," *IEEE Trans. Energy Convers.*, Vol. 35, No. 3, 1688–1696, 2020.
16. Qu, H., Z. Zhu, and B. Shuang, "Influences of PM number and shape of spoke array pm flux reversal machines," *IEEE Trans. Energy Convers.*, Vol. 36, No. 2, 1131–1142, Jun. 2021.
17. Jing, L., W. Tang, W. Liu, Y. Rao, C. Tan, and R. Qu, "A double-stator single-rotor magnetic field modulated motor with HTS bulks," *IEEE Trans. Appl. Supercond.* Vol. 32, No. 6, 1–5, 2022.
18. Qu, H., Z. Zhu, and H. Li, "Analysis of novel consequent pole flux reversal permanent magnet machines," *IEEE Trans. Ind. Appl.*, Vol. 57, No. 1, 382–396, Jan. 2021.
19. Gao, Y., R. Qu, D. Li, J. Li, and L. Wu, "Design of three-phase flux-reversal machines with fractional-slot windings," *IEEE Trans. Ind. Appl.*, Vol. 52, No. 4, 2856–2864, 2016.
20. Tang, W., L. Jing, and L. Zheng, "A diesel-electric hybrid field modulation motor with bread-loaf eccentric magnetic pole for ship propulsion," *Progress In Electromagnetics Research C*, Vol. 125, 147–159, 2022.
21. Jing, L., W. Tang, T. Wang, T. Ben, and R. Qu, "Performance analysis of magnetically geared permanent magnet brushless motor for hybrid electric vehicles," *IEEE Trans. Transp. Electr.*, Vol. 8, No. 2, 2874–2883, Jun. 2022.